# Matching of Physical Experiments and Multibody Dynamic Simulation for Large Deformation Problems

**Wan-Suk Yoo*, Jeong-Han Lee, Jeong-Hyun Sohn, Su-Jin Park**
*CAELab, NRL, Pusan National University, Kumjung-Ku, Busan 609-735, South Korea*
**Oleg Dmitrochenko, Dmitri Pogorelov**
*Bryansk State Technical University, Bryansk 241035, Russia*

Many papers have studied computer simulations of elastic bodies undergoing large deflections and large deformations. But there have not been many attempts to check the validity of the numerical formulations because the simulation results could not be matched without correct input data such as material properties and damping effects. In this paper, these values are obtained from real experiment with a high-speed camera and a data acquisition system. The simulation results with the absolute nodal coordinate formulation (ANCF) are compared with the results of real experiments. Two examples, a thin cantilever beam and a thin plate, are studied to verify whether the simulation results are well matched to experimental results.

**Key Words :** Large Displacements, Experiments, Simulation, Absolute Nodal Coordinate Formulation

## 1. Introduction

The absolute nodal coordinate formulation (ANCF) was known a nice technique for modeling and simulation of large deformation and large displacement problems (Omar and Shabana, 2001). In this formulation, displacements of each finite element are represented relative to the global frame of reference. And the equations of motion with this formulation generate a constant mass matrix and a constant vector of generalized gravity forces as well as zero centrifugal and Coriolis forces (Mikkola and Shabana, 2001). Thus, the only nonlinear term in the equations of motion is the vector of elastic forces.

Although this formulation is widely used for simulations of large deformation problems with nice animations, no paper was written concerning the validity of these simulations by comparing with real experiments. Without correct input data, such as air damping in the motion, the simulation could not be well matched to the experimental results. Thus, in this paper, Young's modulus E and the damping ratio of the material used in the simulation are obtained from the real experiments. Thus, the precise validation of the ANCF could be checked. For the author's knowledge, this is the first paper to compare the ANCF formulation to real experiments. Two experiments, a 2D beam deflection and a thin plate oscillation, are carried out and compared to show the validity of the simulations.

For the modeling of a 2D beam, many models of elastic forces have been proposed which use a matrix representation of the beam shape functions and nodal coordinates (Craig, 1981). In this paper, a new geometrical treatment of the absolute nodal coordinates is suggested. Nodal displacements and nodal slopes are employed for the finite element formulation. The position of an arbitrary point in the beam centerline is then expressed as a linear combination of the nodal

* Corresponding Author,
**E-mail** : wsyoo@pusan.ac.kr
**TEL** : +82-51-510-2328; **FAX** : +82-51-512-9835
CAELab, NRL, Pusan National University, Kumjung-Ku, Busan 609-735, South Korea. (Manuscript **Received** February 22, 2003; **Revised** February 2, 2004)

vectors with the shape functions used as coefficients. This approach is identical to the matrix representation proposed in paper (Bathe, 1996), but it avoids the problem of using zero values for the shape function matrix. Strain energy, elastic forces and their Jacobian matrices are calculated explicitly using tensor-like relations.(Lee, 2003) For a modeling of a thin plate, a 48 d.o.f. plate element is developed with a two-dimensional beam×beam plate element. The element is the direct generalizations of 16 d.o.f. element usually used in the finite element method. The Kirchhoff plate theory with nonlinear strain-displacement relationships was used to calculate elastic forces as well as differential geometry of surfaces in 3D space to calculate mid-plane deformations and transverse curvatures and twist.

For the modeling of material damping and air resistant damping, the Rayleigh's proportional damping was employed to account for resistance forces. To choose the constants in the proportional damping, we carried out oscillations of a cantilever beam and a thin plate with an end-point weight attached. Furthermore, we obtained experimental data on the large deflections of a 2D beam and a thin plate to verify the results generated by ANCF.

To the best of the authors' knowledge, this paper is the first to compare data from simulations and real experiments on large deformations of beams.

The paper is organized as follows. A description of our experimental setup for a beam is explained in chapter 2, and the formulation and simulation of 2D beam in chapter 3. In chapter 4, results from the experiments and computer simulations of a beam are compared. An experimental setup for a plate is explained in chapter 5, and the formulation and simulation of a plate is in chapter 6. Results from the experiments and computer simulations of a plate are compared in chapter 7, and the conclusions are listed.

## 2. Experiments of Large Deflection of 2D Beam

The large deflection experiments of a beam focus on the motion of a cantilever beam with a weight attached to the free end as presented in Fig. 1.

### 2.1 Experimental setup with a high speed camera

An accelerometer is usually used to measure accelerations and displacements. However, the beam used in this research is too thin to install an accelerometer. Therefore, a high-speed camera (REDLAKE Motion Scope type), which runs up 1000 frames per second, is used to measure motion.

The beam used in this test has diameter of 1 mm, length of 400 mm, and are made of industrial spring steel. To make it a cantilever, the

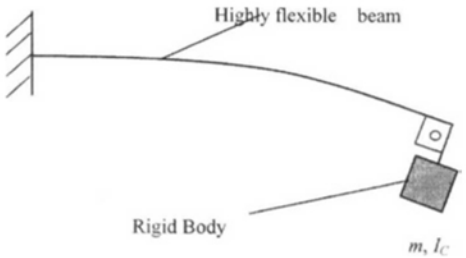


**Fig. 1** Cantilever beam with attached mass

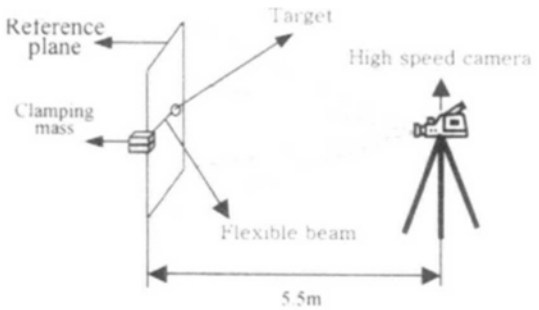


(a) Location of high-speed camera

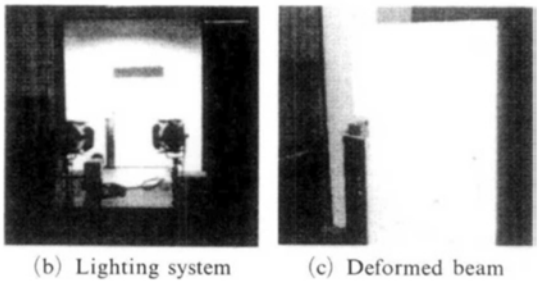

(b) Lighting system (c) Deformed beam

**Fig. 2** Experimental setup

beam is clamped tightly by a heavy jig, and is held in place by two thick steel blocks. The mass of the clamp is 1.74 kg, which is 1700 times heavier then the mass of the beam. Moreover, the clamp is secured with 4 bolts, which ensures a cantilever beam.

To track the end point deflection, a tracking mark was bonded at the tip. The experimental setup was installed as shown in Fig. 2, and deflections were captured by a high-speed camera.

### 2.2 Free vibration to calculate Young's modulus and damping ratio

The stiffness of the beam (i.e., Young's modulus E), which is its most important material property, is calculated by an indirect method rather than a tensile test. Because the beam is too thin to fix at the tester, it is difficult to conduct such a test properly. Therefore the beam's stiffness is calculated using its measured first mode and its density. The first step is to measure the deflection of beam; the second is to calculate the first frequency of the cantilever beam. The third one calculates the stiffness using relationship between the frequency and the material's properties. The first frequency for the beam was obtained from the FFT of the free vibration, which is shown in Fig. 3. From the Fig. 3, the first frequency of the beam is obtained as 4.315 Hz.

The stiffness of the beam can be calculated from the frequency of the first mode as seen in (Meirovitch, 1982)

$$\omega=(\beta l)^2\sqrt{\frac{EI}{\rho Al^4}} \tag{1}$$

where $\beta l$ represents the boundary conditions of the beam. The stiffness can then be calculated according to the formula found:

$$E=\frac{\omega^2}{(\beta l)^4}\rho Al^4\frac{1}{I} \tag{2}$$

The calculated value $E$ of the 1 mm diameter beam was 200 GPa. Next, the damping ratio must be calculated for the simulation. To model the damping, a particular form of proportional Rayleigh damping (Bathe, 1996) is employed and the system damping matrix assumes the following form:

$$\mathbf{D}=\alpha\mathbf{M}+\beta\mathbf{C} \tag{3}$$

which includes the mass matrix $\mathbf{M}$ and the stiffness matrix $\mathbf{C}$ multiplied by the coefficients defined below:

$$\alpha=\frac{2\omega_1\omega_2(\zeta_1\omega_2-\zeta_2\omega_1)}{\omega_2^2-\omega_1^2}$$
$$\beta=\frac{2(\zeta_2\omega_2-\zeta_1\omega_1)}{\omega_2^2-\omega_1^2} \tag{4}$$

which themselves depend on the frequencies $\omega_1$ and $\omega_2$, as well as on the damping ratio $\zeta_1$ and $\zeta_2$ for the first two modes of the system that appear from the dynamic modal equations:

$$\ddot{x}_i+2\zeta_i\omega_i\dot{x}_i+\omega_i^2x_i=0.$$

The ratios $\zeta_1$ and $\zeta_2$ should be calculated from the experimental data. The damping ratio of the first mode is calculated in accordance with the formula from reference (Meirovitch, 1982; Takahashi et al., 2002).

$$\zeta_1=\frac{\delta_1}{2\pi}\left(1+\frac{\delta_1}{2\pi}\right)^{-1/2}$$

where $\delta_1$ is the logarithmic decrement. In case of low-level damping (such as this one), when $\delta_1\ll 2\pi$, we can use the simplified expression

$$\zeta_1\approx\frac{\delta_1}{2\pi}.$$

The logarithmic decrement $\delta_1$ can be estimated from the experimental sequence of magnitudes using the simple relationship below.

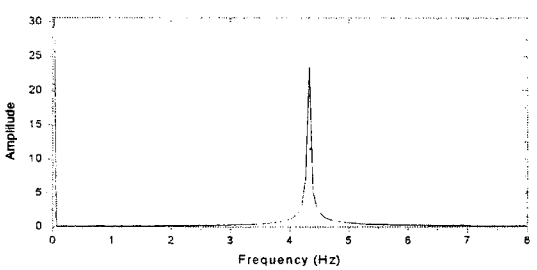


**Fig. 3** The first frequency of 1 mm beam

$$\delta_1=\ln \Delta_1,\ \Delta_1\approx\left(\frac{A_n}{A_1}\right)^{\frac{1}{n-1}} \tag{5}$$

where $A_1$ and $A_n$ are peaks of the first and nth oscillations from the release test.

Since $\omega_2$ could not be captured by a release test, an impact test was used to find $\omega_2$ by impacting the end point. The value $\zeta_2$ was calculated the same method used for the first mode.

### 2.3 Large deformation of 2D beam

A measured mass was attached to the end of a beam to induce large deformation and a circular target point was glued on to track the beam's displacement. The mass at the end of the beam is supported until the test begins: it is released when the camera starts rolling.

The shape and location of the attached mass are shown in Fig. 4, and the parameters of the various objects used in this test are provided in Table 1.

Since the paper target's mass is very small, its effect on the results of the large deformation test is negligible. However, for the deflection without attached mass, the target's mass should be considered. A photograph of a large deformation of the beam is shown in Fig. 5. Not surprisingly it shows much deformation due to effect of the attached mass. The results of the endpoint deflections are measured 336 mm, and the natural frequency of the beam was found 1.204 Hz by using the FFT process.

The maximum displacement in the vertical direction is about 86% of the beam's length. The shapes and chronologies of these deformations are presented in Fig. 6.

After conducting the test of large deformation, the beams were retested to measure their plastic deformation. As the beams returned back to their original positions when the attached masses are removed, there was no plastic deformation.

**Table 1** End-body parameters

| Body No. | Descrip Tion | $m_0$ mass g | Shift of mass center, mm | | $I_C$ mass inertia moment kg·m² |
|---|---|---|---|---|---|
| | | | $\rho_{Cx}$ | $\rho_{Cy}$ | |
| 1 | paper tar get | 0.023 | 0 | 0 | $\sim 10^{-10}\approx 0$ |
| 2 | Attached mass | 20.0 | 0 | −13 | $1.58\cdot 10^{-6}$ |

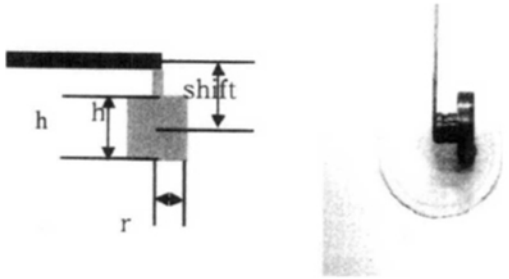


**Fig. 4** Attached mass

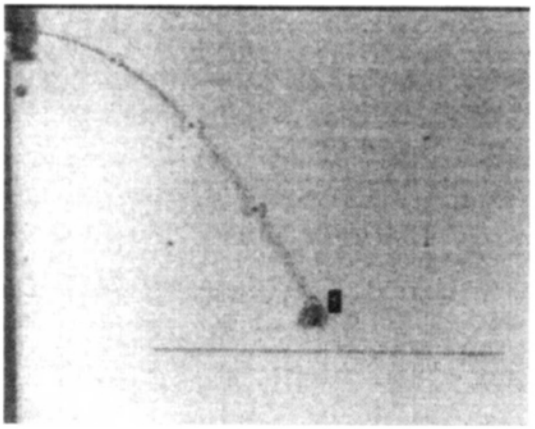

**Fig. 5** A beam after a test of large deformation

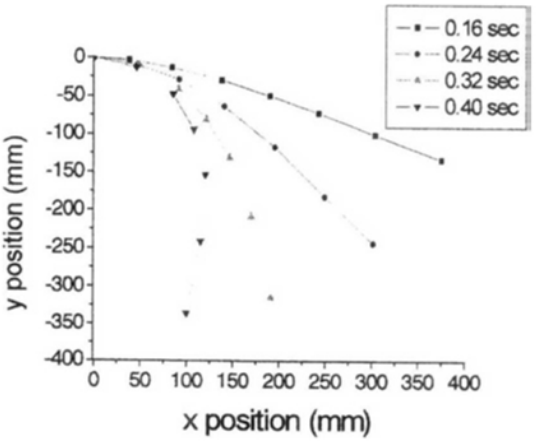


**Fig. 6** Shapes and chronologies of the large deformations (1 mm diameter, 20 g attached mass)

## 3. Finite Element Model and Simulation of Large Deflection of 2D Beam

A brief explanation about the 2D beam simulation with absolute nodal coordinate formulation is explained here. More detailed derivation and simulation are explained in the reference (Yoo et al., 2003).

Consider a finite element of the 2D Euler-Bernoulli beam shown in Fig. 7. The line running through its center is parameterized by the value $p=0, \cdots, l$, where $l$ is the beam's initial length. The vector of the absolute nodal coordinates contains position vectors $\mathbf{r}_0$, $\mathbf{r}_l$ (of the end points) and the tangent slope vectors $\tau_0$, $\tau_l$ at these points.

We use the following index notation for the vector of the absolute nodal coordinates of the beam:

$$\mathbf{e}=\begin{Bmatrix}\mathbf{r}_0\\ \tau_0\\ \mathbf{r}_l\\ \tau_l\end{Bmatrix}=\begin{Bmatrix}\mathbf{e}_1\\ \mathbf{e}_2\\ \mathbf{e}_3\\ \mathbf{e}_4\end{Bmatrix}.$$

It can be shown that the position of an arbitrary point on the element is given by the following formula (Yoo et al., 2003):

$$\mathbf{r}(p)=\begin{bmatrix}s_1 & 0 & s_2 & 0 & s_3 & 0 & s_4 & 0\\ 0 & s_1 & 0 & s_2 & 0 & s_3 & 0 & s_4\end{bmatrix}\begin{Bmatrix}\begin{Bmatrix}r_{0x}\\ r_{0y}\end{Bmatrix}\\ \vdots\\ \begin{Bmatrix}\tau_{lx}\\ \tau_{ly}\end{Bmatrix}\end{Bmatrix}$$

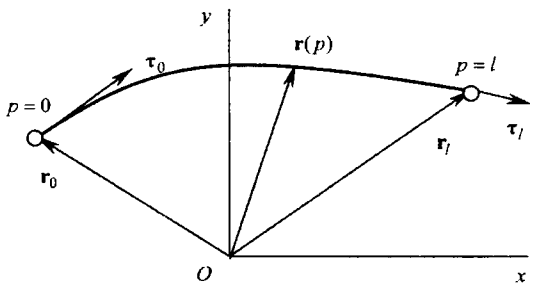


**Fig. 7** 2D beam finite element

with global shape functions defined as follows:

$$s_1=1-3\xi^2+2\xi^3,\ s_2=l(\xi-2\xi^2+\xi^3),\quad \xi=p/l.$$
$$s_3=3\xi^2-2\xi^3,\quad s_4=l(\xi^3-\xi^2),$$

For the sake of simplicity, however, we will use slightly different notation to express the same thing:

$$\mathbf{r}(p)=[s_1\mathbf{I}\ s_2\mathbf{I}\ s_3\mathbf{I}\ s_4\mathbf{I}]\begin{Bmatrix}\mathbf{e}_1\\ \mathbf{e}_2\\ \mathbf{e}_3\\ \mathbf{e}_4\end{Bmatrix}=\sum_{k=1}^{4}s_k\mathbf{e}_k \qquad (6)$$

Thus according the use of many zero values in our matrix computations. $\mathbf{I}$ represents the $2\times2$ identity matrix. More detailed explanations can be found in reference (Dmitrochenko, 2002).

The equations of motion of the beam element can be obtained from the following Lagrange equations

$$\frac{d}{dt}\left(\frac{\partial T}{\partial \dot{\mathbf{e}}}\right)^T-\left(\frac{\partial T}{\partial \mathbf{e}}\right)^T+\left(\frac{\partial U}{\partial \mathbf{e}}\right)^T=\left(\frac{\delta W}{\delta \mathbf{e}}\right)^T$$

where kinetic energy $T$ is defined by the equation $T=\frac{1}{2}\int_0^l \mu\dot{\mathbf{r}}^T\dot{\mathbf{r}}dp$, $U$ represents strain energy. And the virtual work of external gravity forces is given by $\delta W=\int_0^l \delta\mathbf{r}^T\mu\mathbf{g}dp$, where $\mu$ is the linear density in kg/m. These equations assume the matrix form:

$$\mathbf{M}\ddot{\mathbf{e}}+\mathbf{Q}^e=\mathbf{Q}^g \qquad (7)$$

where

$$\mathbf{M}=\frac{\mu l}{420}\begin{bmatrix}156\mathbf{I} & & & sym.\\ 22l\mathbf{I} & 4l^2\mathbf{I} & 156\mathbf{I} & \\ 54\mathbf{I} & 13l\mathbf{I} & -22l\mathbf{I} & \\ -13l\mathbf{I} & -3l^2\mathbf{I} & & 4l^2\mathbf{I}\end{bmatrix}$$

$$\mathbf{Q}^e=\begin{Bmatrix}\mathbf{Q}_1^e\\ \mathbf{Q}_2^e\\ \mathbf{Q}_3^e\\ \mathbf{Q}_4^e\end{Bmatrix},\quad \mathbf{Q}^g=\begin{Bmatrix}\mu\mathbf{g}l/2\\ \mu\mathbf{g}l^2/12\\ \mu\mathbf{g}l/2\\ -\mu\mathbf{g}l^2/12\end{Bmatrix}$$

For the modeling of an attached mass, an element using nodal slopes as generalized coordinates was used. More detail derivation can be found in the reference (Yoo et al., 2003).

The equations of motion formulated in this investigation were put in the Universal Mechanism (UM) program in reference (Pogorelov, 1997) to obtain the solution.

## 4. Comparison of Simulation and Experiment with 2D Beam

Let us perform these calculations for the following case: the beam with diameter $d=1$ mm and end-point mass $m_0=20$ g of the target. With the following values from experiments, $\omega_1=6.7$ rad/s, $\omega_2=33$ rad/s, $\Delta_1=0.987$, and $\zeta_1=\zeta_2=0.002$, constants $\alpha$ and $\beta$ are calculated as $\alpha=0.02\ s^{-1}$, $\beta=1\cdot10^{-5}s$, respectively. One can see that the value of $\beta$ is much smaller than that of $\alpha$. It is thus natural to try to ignore the stiffness-proportional part of the damping forces (Bathe, 1996) and use the simpler damping matrix:

$$\mathbf{D}=\alpha\mathbf{M} \tag{8}$$

Numerical integration shows that the results obtained by both models and equation (8) differ only in $4^{th}$-$5^{th}$ significant digits. However, the integration step in the case of the full damping matrix produces a value that is 20 times smaller because the equations of motion are much stiffer in that case. This is why the simplified model of damping forces (8) is used in the numerical examples below. As can be seen in Fig. 8, the simulation result shows a nice agreement.

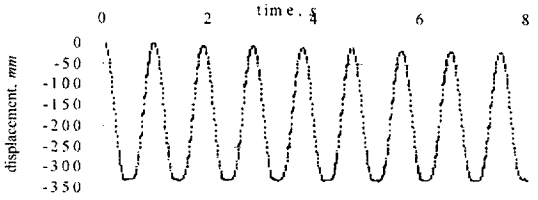


**Fig. 8** Comparison of experiments and simulation

## 5. Experiments of a Thin Plate Oscillation

This section focuses on the large motion of a thin plate with a weight attached to the free end.

### 5.1 Experimental results of a plate

The experimental setup for the plate oscillation is shown in Fig. 9. The camera traces the target fixed at the tip. Since the motion occurs in a three dimensional space, the distance from the camera to the target is changing when the deflection occurs. Thus, the camera is installed as far as possible to reduce this kind of visual distance error. Since the camera is installed 10 m from the target in the experiments, the maximum error is less then 2.5% when the deflection is about 25 mm.

The tip position of a 400 mm×204 mm×0.4 mm plate with 400 g of attached mass is shown in Fig. 10, and the $x$, $y$, and $z$ positions in time domain are shown in Fig. 11.

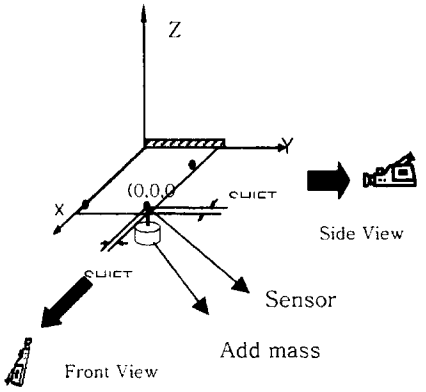


**Fig. 9** Experimental setup for a thin plate

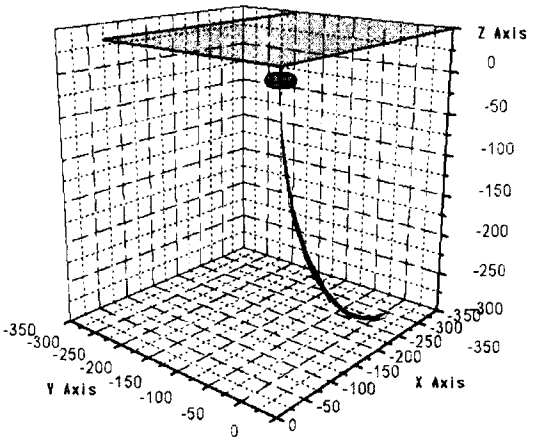


**Fig. 10** Tip position in space

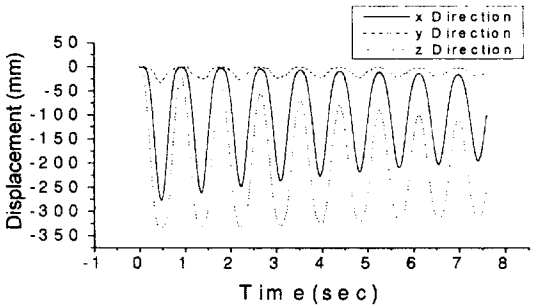


**Fig. 11** Tip positions in time domain

### 5.2 Frequency and damping ratio for the simulation

To verify the natural frequencies and damping ratio of the plate, the vertical displacement of the plate with attached mass is measured, which is shown in Fig. 12. The transformed signals by FFT are shown in Fig. 13. The first and the second modes are clearly shown, and the first modal frequency is about 1.2 Hz. From this value of frequency, the Young's modulus E of the plate is calculated and used for the input data in the computer simulation.

Damping ratio of the plate is calculated by the following formula by using $z_1$ and the $z_{n+1}$ values in Fig. 12 and the $\omega_n$ value in Fig. 13.

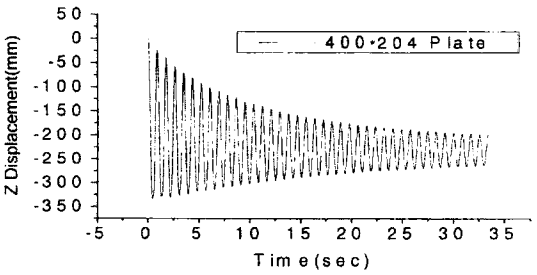


**Fig. 12** Ocillation of the plate

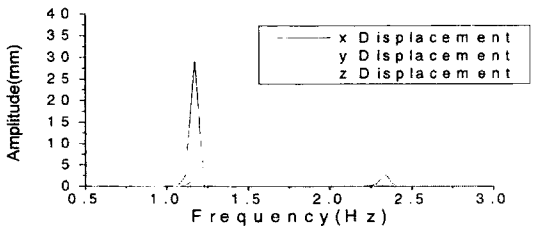


**Fig. 13** Natural frequency of the plate

$$\zeta=\frac{1}{\omega_n m\tau_d}\ln\frac{z_1}{z_{n+1}}=\frac{1}{\omega_n(t_{n+1}-t_1)}\ln\frac{z_1}{z_{n+1}}$$

where $z_1$ and $z_{n+1}$ are peaks of the first and nth oscillations in Fig. 12.

## 6. Finite Element Formulation and Simulation of a Plate Using ANCF

### 6.1 Finite element model of a plate

In this chapter, EOM (equations of motion) of a thin plate are formulated with ANCF (absolute nodal coordinate formulation) and the simulations are carried out with the derived formulation. With a two-dimensional beam×beam plate element (Dmitrochenko, 2001), a 48 dof (degrees of freedom) plate element is developed. A beam× beam plate element is a four-node plate element, each node has 12 dofs (degrees of freedom). Twelve dofs consist one position vector and three rotation vectors in a 3-dimensional space.

The Kirchhoff plate theory with nonlinear strain-displacement relationships was used to calculate elastic forces as well as differential geometry of surfaces in 3D space to calculate mid-plane deformations and transverse curvatures and twist.

The proposed element is able to correctly represent large overall motion because its shape functions contain a full set of rigid-body modes. It also can represent large deformation due to nonlinear strain-displacement relationships used in this investigation.

Let us consider a plate element of size $a\times b\times h$ (length×width×thickness). The plate is represented by its middle surface only, as shown in Fig. 14.

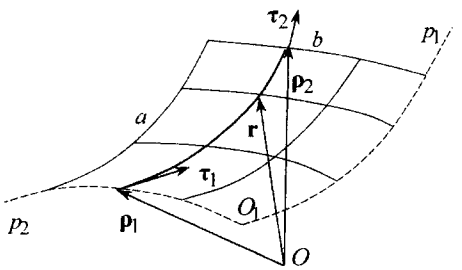


**Fig. 14** Beam-beam model of a plate

The surface of the plate is parameterized by values $p_1$ and $p_2$. Let $O_1$ be the origin of the configuration space of the element. Let us imagine a coordinate curve parallel to axis $p_1$ ($p_1$-beam) to define the position $\mathbf{r}(p_1, p_2)$ of an arbitrary point of the plate relative to the origin $O$ of the inertial reference frame. Extension of the idea of absolute nodal coordinate formulation for 3D beams gives;

$$\mathbf{r}(p_1, p_2)=[\hat{s}_1\mathbf{I}\ \hat{s}_2\mathbf{I}\ \hat{s}_3\mathbf{I}\ \hat{s}_4\mathbf{I}]\begin{Bmatrix}\boldsymbol{\rho}_1\\ \boldsymbol{\tau}_1\\ \boldsymbol{\rho}_2\\ \boldsymbol{\tau}_2\end{Bmatrix} \tag{9}$$

where $\hat{s}_k=s_k(p_1, l)$ are Hermite shape functions for the $p_1$-beam:

$$\begin{aligned}&s_1(p, l)=s_3(l-p, l)=1-3\xi^2+2\xi^3,\\ &s_2(p, l)=-s_4(l-p, l)=l(\xi-2\xi^2+\xi^3),\\ &s_3(p, l)=3\xi^2-2\xi^3,\\ &s_4(p, l)=l(\xi^3-\xi^2)\end{aligned}\qquad \xi=\frac{p}{l}.$$

$\mathbf{I}$ is the $3\times3$ identity matrix, $\boldsymbol{\rho}_k$ and $\boldsymbol{\tau}_k$ are absolute nodal coordinates of the $p_1$-beam (global displacements and slopes of the end points).

### 6.2 Mass matrix and equations of motion of a plate

To derive dynamic equations of a plate element, we employ Lagrange equations in a matrix representation

$$\frac{d}{dt}\left(\frac{\partial T}{\partial \dot{\mathbf{e}}}\right)^T-\left(\frac{\partial T}{\partial \mathbf{e}}\right)^T+\left(\frac{\partial U}{\partial \mathbf{e}}\right)^T=\left(\frac{\delta W}{\delta \mathbf{e}}\right)^T$$

with kinetic energy $T=\frac{1}{2}\int_0^a\int_0^b \mu\dot{\mathbf{r}}^T\dot{\mathbf{r}}dp_1dp_2$, internal strain energy $U$ and virtual work $\delta W=\int_0^a\int_0^b \delta\mathbf{r}^T\mu\mathbf{g}dp_1dp_2$ of external gravity forces $\mu\mathbf{g}$.

Taking into account relation leads to the equations of motion

$$\mathbf{M}\ddot{\mathbf{e}}+\mathbf{Q}^e=\mathbf{Q}^g \tag{10}$$

with the constant mass matrix $\mathbf{M}=\int_0^a\int_0^b \mu\mathbf{S}^T\mathbf{S}dp_1dp_2$, the surface mass density $\mu$ of the plate, the elastic $\mathbf{Q}^e=\partial U/\partial\mathbf{e}$ and gravity $\mathbf{Q}^g=\overline{\mathbf{S}}^T\mu\mathbf{g}$ generalized forces, $\overline{\mathbf{S}}=\int_0^a\int_0^b \mathbf{S}dp_1dp_2$. Note, that centrifugal and Coriolis inertia forces are absent. This is usual for the absolute nodal coordinate formulation (Mikkola, 2001).

An explicit expression for the mass matrix can be obtained in a block matrix form using definition of the shape function as

$$\mathbf{M}=\begin{bmatrix}\mathbf{M}_{11}&\mathbf{M}_{12}&\mathbf{M}_{13}&\mathbf{M}_{14}\\ \mathbf{M}_{21}&\mathbf{M}_{22}&\mathbf{M}_{23}&\mathbf{M}_{24}\\ \mathbf{M}_{31}&\mathbf{M}_{32}&\mathbf{M}_{33}&\mathbf{M}_{34}\\ \mathbf{M}_{41}&\mathbf{M}_{42}&\mathbf{M}_{43}&\mathbf{M}_{44}\end{bmatrix}$$

$$\mathbf{M}_{ij}=\begin{bmatrix}\mathbf{M}_{ij11}&\mathbf{M}_{ij12}&\mathbf{M}_{ij13}&\mathbf{M}_{ij14}\\ \mathbf{M}_{ij21}&\mathbf{M}_{ij22}&\mathbf{M}_{ij23}&\mathbf{M}_{ij24}\\ \mathbf{M}_{ij31}&\mathbf{M}_{ij32}&\mathbf{M}_{ij33}&\mathbf{M}_{ij34}\\ \mathbf{M}_{ij41}&\mathbf{M}_{ij42}&\mathbf{M}_{ij43}&\mathbf{M}_{ij44}\end{bmatrix}$$

where each block $\mathbf{M}_{ij}$ is also a block matrix with block-elements

$$\mathbf{M}_{ijkl}=M_{ijkl}\mathbf{I}$$

$$\begin{aligned}M_{ijkl}&=\iint_P \mu S_{ik}S_{jl}dp=\mu\iint_P \hat{s}_i\hat{\hat{s}}_k\hat{s}_j\hat{\hat{s}}_l dP\\ &=\mu\int_0^a \hat{s}_i\hat{s}_j dp_1\int_0^b \hat{\hat{s}}_k\hat{\hat{s}}_l dp_2=\mu\hat{\hat{S}}^{00}_{ij}\hat{\hat{S}}^{00}_{kl}.\end{aligned}$$

Matrices with hats are similar to mass matrices for beam.

$$\hat{\hat{S}}^{00}_{ij}=\frac{a}{420}\begin{bmatrix}156&&&sym\\ 22a&4a^2&&\\ 54&13a&156&\\ -13a&-3a^2&-22a&4a^2\end{bmatrix}_{ij}$$

Matrix $\overline{\mathbf{S}}$ is easy to calculate explicitly, too:

$$\begin{aligned}\overline{\mathbf{S}}=[&\overline{S}_{11}\mathbf{I},\ \overline{S}_{12}\mathbf{I},\ \overline{S}_{13}\mathbf{I},\ \overline{S}_{14}\mathbf{I};\ \cdots;\ \cdots;\\ &\overline{S}_{41}\mathbf{I},\ \overline{S}_{42}\mathbf{I},\ \overline{S}_{43}\mathbf{I},\ \overline{S}_{44}\mathbf{I}]\end{aligned}$$

$$\begin{aligned}\overline{S}_{ij}&=\iint_P S_{ij}dP=\iint_P \hat{s}_i\hat{\hat{s}}_j dP\\ &=\int_0^a \hat{s}_i dp_1\int_0^b \hat{\hat{s}}_j dp_2=\hat{\overline{S}}^0_i\hat{\hat{\overline{S}}}^0_j\end{aligned}$$

the symbols with hats being well-known from the beam elements theory. All terms in equation (10) are obtained except elastic forces $\mathbf{Q}^e$, which are the most difficult to calculate due to complexity of the strain energy.

Following the Kirchhoff theory, the strain energy of an orthotropic plate can be decomposed into longitudinal and shear deformations in

the mid-plane, and a transverse one due to its bending and twist:

$$U = U^{\epsilon} + U^{\kappa}$$

$$U^{\epsilon} = \frac{6}{h^2}\iint_P \left( \sum_{i=1}^{2}\sum_{j=1}^{2} D_{ij}\epsilon_{ij}^2 + 2D_{22}^{11}\epsilon_{11}\epsilon_{22} \right) dP \quad (11)$$

$$U^{\kappa} = \frac{1}{2}\iint_P \left( \sum_{i=1}^{2}\sum_{j=1}^{2} D_{ij}\kappa_{ij}^2 + 2D_{22}^{11}\kappa_{11}\kappa_{22} \right) dP \quad (12)$$

The energy contains, firstly, elastic parameters of the material of the plate: flexural rigidities $D_{11}$, $D_{22}$ and twist stiffness $D_{12}$:

$$D_{11} = \frac{E_{11}h^3}{12(1-\nu_{12}\nu_{21})}, \quad D_{22} = \frac{E_{22}h^3}{12(1-\nu_{12}\nu_{21})}$$

$$D_{12} = D_{21} = \frac{E_{12}h^3}{6}$$

and also an additional stiffness coefficient $D_{22}^{11} = 0.5(D_{11}\nu_{21} + D_{22}\nu_{12})$. The latter expressions depend on Young moduli $E_{11}$, $E_{22}$ and a shear modulus $E_{12}$ as well as on Poisson ratios $\nu_{12}$ and $\nu_{21}$. The ratios satisfy the following condition:

$$E_{11}\nu_{21} = E_{22}\nu_{12}$$

Secondly, the strain energy contains geometrical parameters of the plate: longitudinal deformations $\epsilon_{11}$, $\epsilon_{22}$ and shear deformations $\epsilon_{12} = \epsilon_{21}$ as well as transverse curvatures $\kappa_{11}$, $\kappa_{22}$ and a twist $\kappa_{12} = \kappa_{21}$.

In case of small deflections, the deformed surface of the plate is defined by three scalar functions: by mid-plane displacements $u(x, y)$, $v(x, y)$ and by a transverse displacement $w(x, y)$. In that case, the mentioned deformations and curvatures are calculated as follows:

$$\epsilon_{11} = \frac{\partial u}{\partial x}, \quad \epsilon_{22} = \frac{\partial \nu}{\partial y}, \quad \epsilon_{12} = \frac{1}{2}\left( \frac{\partial u}{\partial y} + \frac{\partial \nu}{\partial x} \right)$$

$$\kappa_{11} = \frac{\partial^2 w}{\partial x^2}, \quad \kappa_{22} = \frac{\partial^2 w}{\partial y^2}, \quad \kappa_{12} = \frac{\partial^2 w}{\partial x \partial y}.$$

In our case when the plate is oriented in an arbitrary way and specified in a parameterized form $\mathbf{r} = \mathbf{r}(p_1, p_2)$, we should use the relationships from differential geometry of surfaces. Then we obtain expressions for deformations in the mid-plane of the plate

$$\epsilon_{ij} = \frac{1}{2}(\mathbf{r}_i^T\mathbf{r}_j - \delta_{ij}) \quad (13)$$

with a Kronecker symbol $\delta_{ij}$ as well as for transverse curvatures and twist

$$\kappa_{ij} = \mathbf{r}_{ij}^T\mathbf{n}/\|\mathbf{n}\|^3 \quad (14)$$

with the normal vector $\mathbf{n} = \mathbf{r}_2 \times \mathbf{r}_2$. Other notations are the derivatives

$$\mathbf{r}_i = \frac{\partial \mathbf{r}}{\partial p_i} = S_{mn}^i \mathbf{e}_{mn}, \quad \mathbf{r}_{ij} = \frac{\partial^2 \mathbf{r}}{\partial p_i \partial p_j} = S_{mn}^{ij}\mathbf{e}_{mn} \quad (15)$$

$$\mathbf{r} = \mathbf{u}^* + \mathbf{u} = \begin{Bmatrix} p_1 \\ p_2 \\ 0 \end{Bmatrix} + \begin{Bmatrix} u_1(p_1, p_2) \\ u_2(p_1, p_2) \\ u_3(p_1, p_2) \end{Bmatrix}$$

$$\epsilon_{ij} = \frac{1}{2}\left( \frac{\partial u_i}{\partial p_j} + \frac{\partial u_j}{\partial p_i} + \sum_{k=1}^{3} \frac{\partial u_k}{\partial p_i}\frac{\partial u_k}{\partial p_j} \right)$$

$$\kappa_{ij} = \frac{\partial^2 u_3}{\partial p_i \partial p_j}\left( 1 + \left( \frac{\partial u_3}{\partial p_1} \right)^2 + \left( \frac{\partial u_3}{\partial p_2} \right)^2 \right)^{-\frac{3}{2}}$$

More detail calculation process of longitudinal elastic forces and transverse elastic forces are explained in reference (Yoo et al., 2003).

## 7. Comparison of Simulations and Experiments of a Thin Plate

Figure 15 presents the results for the 400 mm × 204 mm × 0.4 mm plate with 400 g of attached mass. The simulation results and experimental results are compared in Fig. 15. As shown in Fig. 15, $x$ and $z$ positions are in a good agreement. After a few seconds, there are some time lags between two results. The reason, the authors suppose, may came from the values of Young's modulus and damping ratio but the differences are not too big.

The $y$ position shows some deviations, but it is not a big deal if one verifies that the maximum magnitude of the $y$-directional deflection is very small.

Thus, the large deflection simulation of a beam with ANCF formulation and the experimental results are also in a good agreement.

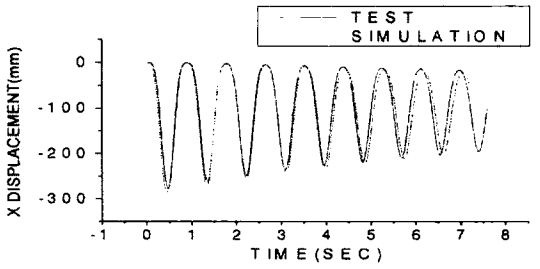


(a) $x$ positions

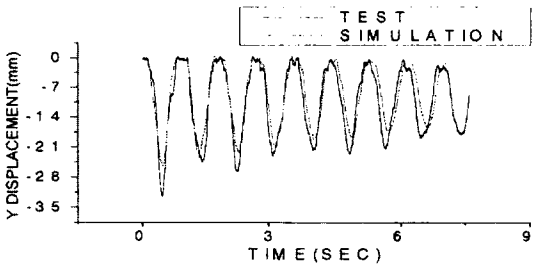


(b) $y$ positions

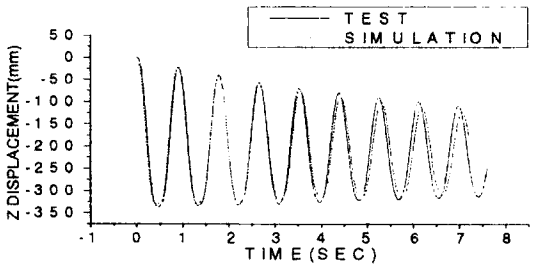


(c) $z$ positions

**Fig. 15** Comparison of experiments and simulation (plate, tip mass 400 g)

## 8. Conclusions

In this paper, experiments and simulations of a 2D cantilever beam and a thin plate with an attached end-point weight are compared. To input a precise data for the material damping and air resistant damping in the simulation, we carried out several experiments.

Rayleigh's proportional damping was applied to account for resistance forces in large oscillation cases. It was found that when such resistance forces are small, it is possible to ignore the stiffness-proportional part of the damping forces and focus exclusively on the mass-proportional part.

To the best of the authors' knowledge, this is the first paper to compare the results of simulations and experiments in this context. Thus we have obtained some new results during this investigation.

We used the ANCF (absolute nodal coordinate formulation) for modeling of 2D beam and suggested a vector-algebra notation for the components of the vector of the nodal coordinates. To simulate the plate oscillation, we developed a new 48 dof plate element from beam×beam element. The comparison of simulation to experiment with a thin plate oscillation also showed a nice agreement.

## Acknowledgment

The authors would like to thank the Ministry of Science and Technology of Korea for its financial support through a grant (M1-0203-00-0017) under the NRL (National Research Laboratory) project.

## References

Bathe, K. J., 1996, Finite Element Procedures, in Engineering Analysis Prentice Hall, New Jersey.

Craig, R. R., 1981, Structural Dynamics.

Dmitrochenko, O. N., 2002, "Efficient Simulation of Rigid-Flexible Multibody Dynamics: Some Implementations and Results," in *Proceedings of NATO ASI on Virtual Nonlinear Multibody Systems* 1, W. Schielen and M. Valášek (Eds.), Prague, pp. 51~56.

Dmitrochenko, O. N., 2001, "Methods of Simulating Dynamics of Hybrid Multibody Systems with Taking into Account Geometrical Nonlinearity," in *Dynamics, strength and reliability of transport machines*, B. G. Keglin (Ed.), Bryansk State Technical University, Bryansk, pp. 24~34 (in Russian).

Lee, J., 2003, "In-Plane Free Vibration Analysis of Curved Timoshenko Beams by the Pseudo-spectral Method," KSME International Journal, Vol. 17, No. 8, pp. 1156~1163.

Meirovitch, L., 1982, Analytical Methods in Vibrations, Macmillan Publishing Co., Inc., New

York.

Mikkola, A. M. and Shabana, A. A., 2001, "A New Plate Element based on the Absolute Nodal Coordinate Formulation," in Proceedings of ASME 2001 DETC, Pittsburgh.

Omar, M. A. and Shabana, A. A., 2001, "A Two-Dimensional Shear Deformation Beam for Large Rotation and Deformation," in Journal of Sound and Vibration 243 (3), pp. 565～576.

Pogorelov, D., 1997, "Some Developments in Computational Techniques in Modeling Advanced Mechanical Systems," in *Proceedings of IUTAM Symposium on Interaction between Dynamics and Control in Advanced Mechanical Systems*, D. H. van Campen (Ed.), Kluwer Academic Publishers, Dordrecht, pp. 313～320.

Takahashi, Y., Shimizu, N. and Suzuki, K., 2002, Introduction of Damping Matrix into Absolute Nodal Coordinate Formulation, Proceedings of ACMD '02, pp. 33～40.

Wan-Suk Yoo, Jeong-Han Lee, Jeong-Hyun Sohn, Su-Jin Park, Oleg Dmitrochenko and Dmitri Pogorelov, 2003, "Large Oscillations of a Thin Cantilever Beam : Physical Experiments and Simulation using Absolute Nodal Coordinate Formulation," Nonlinear Dynamics Journal, 34, pp. 3～29.

Wan-Suk Yoo, Jeong-Han Lee, Jeong-Hyun Sohn, Su-Jin Park, Oleg Dmitrochenko and Dmitri Pogorelov, 2003, "Large Deflection Analysis of a thin plate with ANCF : Computer Simulation and Experiments," Proceeding of ECCOMAS Thematic Conference Multibody 2003, Lisbon, Portugal.